Aalborg Universitet

AALBORG UNIVERSITY
DENMARK

Two-port-network-based decoupled impedance modeling method of DFIG system and DC-link coupling analysis

Huang, Liang; Wu, Chao; Zhou, Dao; Blaabjerg, Frede

Link to publication from Aalborg University

Two-port-network-based decoupled impedance modeling method of DFIG system and DC-link coupling analysis

Liang Huang [a,*], Chao Wu [b], Dao Zhou [a], Frede Blaabjerg [a]

[a] *Aalborg University, Pontoppidanstraede 101, Aalborg 9220, Denmark*
[b] *Shanghai Jiao Tong University, No.800 Dongchuan Road, Shanghai 200240, China*

ABSTRACT

The doubly-fed induction generator (DFIG) has been widely used in the field of wind generation. However, due to the couplings on both dc-side and ac-side, the full-order small-signal impedance model of the DFIG system is hard to build. A conventional modeling method is assuming a constant dc-link voltage to ignore the dc-side coupling. However, the reasonability of this assumption has not been demonstrated sufficiently. Differently, this paper proposes a two-port-network-based impedance modeling method by decoupling the ac-side coupling. With this method, the total admittance of the DFIG system is decomposed into four admittance components listed in a two-by-two matrix, and each of them can be calculated independently. Then, a full-order small-signal admittance model can be obtained by adding these four admittance components. The main advantage of the proposed method is that the complexity of the modeling process can be degraded and the impact of the dc-link coupling on the whole DFIG system can be analyzed quantitatively. It is found that only when the magnitudes of the non-diagonal elements in the two-by-two admittance matrix are at least 10 dB lower than the magnitudes of the total admittance of the DFIG system, the dc-link coupling can be ignored. Otherwise, ignoring the dc-link coupling will make the model inaccurate. Admittance measurements in simulations validate the correctness of the proposed modeling method.

1. Introduction

In the past decades, due to the foreseen exhaustion of conventional fossil-based energies and their climate impact, many global efforts have been devoted to developing renewable energy sources [1]. Among numerous renewable energy sources, wind power plays an increasingly important role due to its high energy density and easy obtainment [2]. For example, the on-shore, near-shore, and off-shore wind power have already provided nearly 50 % of the total electricity consumption in Denmark [3]. However, as the penetration of wind power increases, the grid-connected system tends to be unstable [4]. Therefore, modeling and stability analysis for wind power generation systems becomes a hot topic, which attracts a lot of research attention [5–7].

Nowadays, the doubly-fed induction generators (DFIG) and the permanent magnet synchronous generators (PMSG) with back-to-back converters are two mainstream types of wind power generation systems [8,9]. For the PMSG-based wind generation system, the PMSG and the back-to-back converter are connected in series (i.e., linear connection), so that the output impedance model can be easily derived

according to the output voltage and current of the grid-side converter (GSC) [10–12]. Differently, for the DFIG-based wind generation system, the DFIG and the back-to-back converter are connected on both rotor side and stator side (i.e., circular connection), so the DFIG stator currents and the GSC output currents are influenced by each other, which makes it difficult to derive the full-order impedance model of the DFIG system [13–15]. A conventional modeling method is assuming a constant dc-link voltage to ignore the dc-link coupling, so that the rotor-side converter (RSC) and the GSC can be modeled separately [16–21]. However, the reasonability of this assumption has not been demonstrated sufficiently.

Moreover, in order to establish a full-order impedance model of the DFIG system, some improved modeling methods with consideration of the dc-link voltage dynamics have been proposed in [22–24]. In [22], both the GSC and RSC are represented by three-port modules. Then, the full-order impedance model on the ac side can be obtained by combining these two three-port modules, where the dc-side impedance is introduced into the modeling process. However, introducing the dc-side impedance may increase the complexity of the modeling process

---

* Corresponding author.
E-mail address: lihu@energy.aau.dk (L. Huang).

because the final form of the model is the ac impedance rather than the dc impedance. In [23], the dc-link voltage dynamics are described by an indicator function so that a full-order impedance model can be derived in a mathematical way. However, this indicator function may lack a clear physical meaning to show deeper insights. In [24], a detailed sequence impedance modeling method based on the voltage perturbations and current responses is introduced. However, the impact of the dc-link coupling is not identified clearly. Moreover, the critical condition to ignore the dc-link coupling has not been revealed clearly in existing research [22–24]. Thus, when performing the model reduction or simplification in a larger-scale system, the reasonability of the reduced-order model is still questionable.

To address the aforementioned problems, a novel two-port-network-based decoupled impedance modeling method for the DFIG system is proposed in this paper. With this method, the physically coupled DFIG system can be decomposed into four decoupled subsystems and it can be modeled by a 2×2 matrix. Thus, the admittance models of the RSC and the GSC can be represented by the diagonal elements of the matrix, while the dc-link coupling between the RSC and the GSC is able to be reflected by the non-diagonal elements of the matrix. Each of the four elements in the 2×2 matrix can be calculated independently. Then, a full-order small-signal admittance model can be obtained by adding these four elements. Overall, the main contribution of this paper is proposing a two-port-network-based decoupled admittance/impedance modeling method for the DFIG system. Besides, the advantages of the proposed modeling method can be summarized as follows:

(1) The physically coupled DFIG system can be decomposed into four decoupled subsystems for modeling, so the complexity of the modeling process can be degraded.
(2) The admittance models of the four subsystems not only can be calculated but also are able to be measured, so the "white-box" method (i.e., analytical expressions) and the "black-box" method (i.e., measurement) can be used for cross-validation to check the correctness of the four admittance models, as well as the total terminal admittance.
(3) By comparing the admittance models of the GSC, RSC, and the dc-link coupling, it can be figured out which part of the DFIG system has a lower weight. Thus, the model reduction or simplification can be performed accordingly.

Through the quantitative analysis, the critical condition for ignoring the dc-link voltage dynamics can be found, which is that the magnitudes of the admittance model of the dc-link coupling are at least 10 dB lower than the magnitudes of the total admittance of the DFIG system.

The rest of this paper is organized as follows: Section 2 introduces the impedance models of the DFIG + RSC and the GSC respectively. Then, a two-port-network-based decoupled impedance modeling method is proposed in Section 3. After that, the impact of the dc-link coupling is analyzed quantitatively in Section 4. Afterward, comparative analyses based on time-domain simulation results are provided in Section 5. Finally, concluding remarks are drawn in Section 6.

2. Typical impedance modeling of DFIG + RSC and GSC separately

2.1. Configuration of the study system

Schematic diagram of the DFIG-based wind generation system with grid-following control is presented in Fig. 1. Fig. 1(a) shows the physical configuration of the DFIG system, where a DFIG and a back-to-back converter are connected to the grid at the point of common coupling (PCC). C_{dc} is a dc capacitor on the dc-side. L_f and C_f are the filter inductors and capacitors on the ac-side. L_g represents the grid impedance, where the grid resistance is ignored. Considering the rotor speed changes in a slower time scale compared to the fundamental frequency
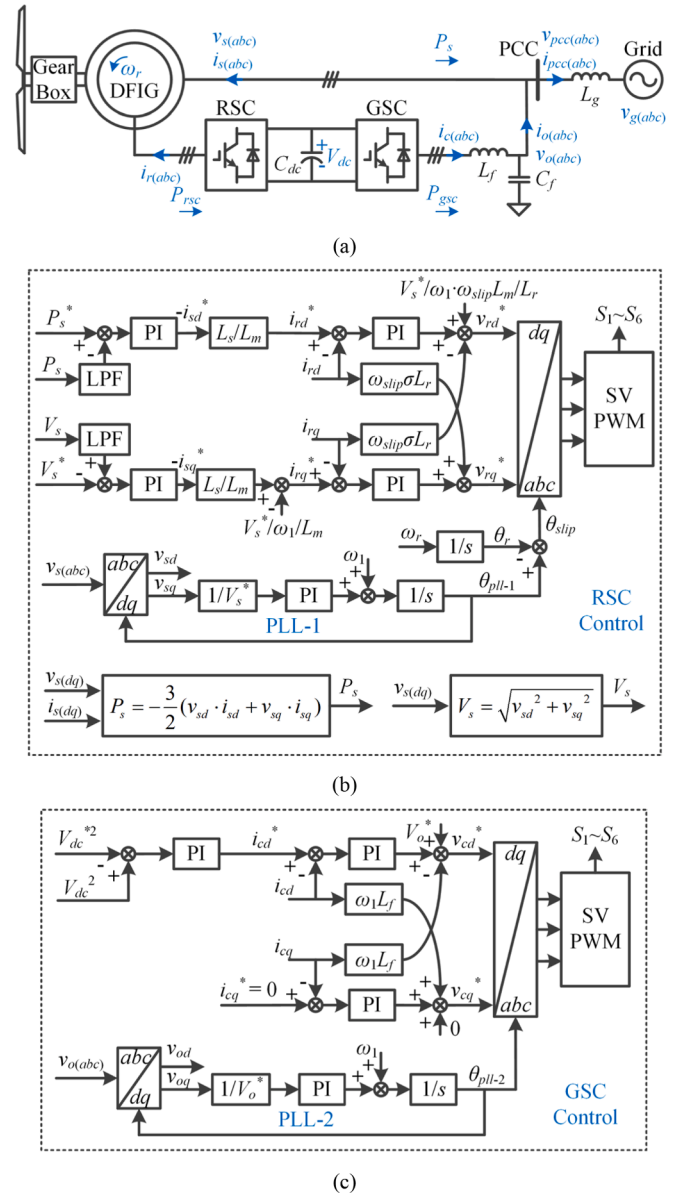

(a)

(b)

(c)

Fig. 1. Schematic diagram of DFIG-based wind generation system with grid-following control. (a) Physical configuration of DFIG system. (b) Control scheme of RSC. (c) Control scheme of GSC.

of the ac voltages and currents, the rotor speed ω_r is assumed to be constant in this paper.

Fig. 1(b) shows the stator-voltage oriented control (SVOC) scheme of the RSC, which includes inner current control loops, outer power control loops and a phase-locked loop (PLL). The control system is performed in the rotating d-q frame. The active power is controlled on the d-axis. In this paper, a weak grid condition with SCR = 1.5 is chosen for study, so the stator voltage magnitude V_s is used for control on the q-axis rather than the reactive power Q_s, which is the same as [25]. In Fig. 1(b), ω_1 represents the angular frequency of the stator voltage, while ω_{slip} represents the slip angular frequency between the stator and the rotor, which is equal to $(\omega_1 - \omega_r)$. Notably, the measured value of dc-link voltage is used for modulation in this paper.

Fig. 1(c) shows the control scheme of the GSC, which includes inner current control loops, an outer dc voltage control loop and a PLL. To differentiate two PLLs on the RSC and GSC, the PLL on the RSC is named "PLL-1", while the PLL on the GSC is named "PLL-2". The detailed small-signal models of DFIG, RSC and GSC will be provided in the following

sections. Notably, the selected control schemes shown in Fig. 1(b) and (c) are just used as an example for analysis in this paper. In other words, the proposed decoupled impedance modeling method (see Section 3) in this paper is not limited to the selected control schemes, which can also be used to build the impedance model of the DFIG system with other control methods (e.g., P and Q control on the RSC [15,26], rotor speed and Q control on the RSC [14], and droop-based power control on the RSC [9]).

2.2. Modeling of DFIG

Same as [16,27], the stator/rotor voltage and flux equations of the DFIG in d-q frame are given by (1)–(4).

$$\begin{cases} v_{sd} = R_s i_{sd} + \dfrac{d\psi_{sd}}{dt} - \omega_1 \psi_{sq} \\[2mm] v_{sq} = R_s i_{sq} + \dfrac{d\psi_{sq}}{dt} + \omega_1 \psi_{sd} \end{cases} \tag{1}$$

$$\begin{cases} v_{rd} = R_r i_{rd} + \dfrac{d\psi_{rd}}{dt} - \omega_{slip} \psi_{rq} \\[2mm] v_{rq} = R_r i_{rq} + \dfrac{d\psi_{rq}}{dt} + \omega_{slip} \psi_{rd} \end{cases} \tag{2}$$

$$\begin{cases} \psi_{sd} = L_s i_{sd} + L_m i_{rd} \\ \psi_{sq} = L_s i_{sq} + L_m i_{rq} \end{cases} \tag{3}$$

$$\begin{cases} \psi_{rd} = L_r i_{rd} + L_m i_{sd} \\ \psi_{rq} = L_r i_{rq} + L_m i_{sq} \end{cases} \tag{4}$$

Substituting (3) and (4) into (2), it can be derived as:

$$\begin{cases} v_{rd} - \dfrac{L_m}{L_s}\dfrac{d\psi_{sd}}{dt} + \dfrac{L_m}{L_s}\omega_{slip}\psi_{sq} = R_r i_{rd} + \sigma L_r \dfrac{di_{rd}}{dt} - \omega_{slip}\sigma L_r i_{rq} \\[2mm] v_{rq} - \dfrac{L_m}{L_s}\dfrac{d\psi_{sq}}{dt} - \dfrac{L_m}{L_s}\omega_{slip}\psi_{sd} = R_r i_{rq} + \sigma L_r \dfrac{di_{rq}}{dt} + \omega_{slip}\sigma L_r i_{rd} \end{cases} \tag{5}$$

where $\sigma = (L_s L_r - L_m^2)/(L_s L_r)$.

Considering the stator resistance R_s in (1) is very small, it can be ignored approximately. Thus, when (1), (3) and (5) are transformed to the frequency domain by using the Laplace transform, the small-signal expressions can be derived as:

$$\begin{bmatrix} \Delta i_{sd} \\ \Delta i_{sq} \end{bmatrix} = \begin{bmatrix} sL_s & -\omega_1 L_s \\ \omega_1 L_s & sL_s \end{bmatrix}^{-1} \cdot \begin{bmatrix} \Delta v_{sd} \\ \Delta v_{sq} \end{bmatrix} - \frac{L_m}{L_s}\begin{bmatrix} \Delta i_{rd} \\ \Delta i_{rq} \end{bmatrix} \tag{6}$$

$$\begin{bmatrix} \Delta i_{rd} \\ \Delta i_{rq} \end{bmatrix} = \begin{bmatrix} R_r + s\sigma L_r & -\omega_{slip}\sigma L_r \\ \omega_{slip}\sigma L_r & R_r + s\sigma L_r \end{bmatrix}^{-1} \cdot \left(\begin{bmatrix} \Delta v_{rd} \\ \Delta v_{rq} \end{bmatrix} \right.$$
$$\left. - \begin{bmatrix} sL_m & -\omega_{slip}L_m \\ \omega_{slip}L_m & sL_m \end{bmatrix} \cdot \begin{bmatrix} sL_s & -\omega_1 L_s \\ \omega_1 L_s & sL_s \end{bmatrix}^{-1} \cdot \begin{bmatrix} \Delta v_{sd} \\ \Delta v_{sq} \end{bmatrix} \right) \tag{7}$$

where Δ represents the small-signal perturbations of variables.

According to (6) and (7), the small-signal impedance model of the DFIG is shown in Fig. 2, where $\mathbf{B_{Lr}}$, $\mathbf{B_{Lm}}$, and $\mathbf{B_{Ls}}$ represent the 2×2 matrixes in (7).
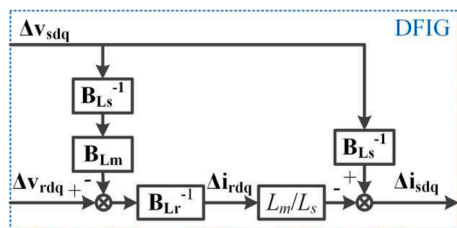
2.3. Modeling of RSC

According to the RSC control scheme in Fig. 1(b), the small-signal impedance model of the RSC is presented in Fig. 3. Notably, each symbol $\mathbf{B}$ represents a 2×2 matrix. The detailed expressions of all the matrixes are provided in the Appendix. Same as [28], to differentiate the system d-q frame and the control d-q frame, a superscript 'ctrl' denotes the variables in the control d-q frame.

2.4. Modeling of GSC

Similarly, according to the GSC control scheme in Fig. 1(c), the small-signal impedance model of the GSC is presented in Fig. 4. The detailed expressions of all the matrixes are given in the Appendix.

3. Proposed two-port-network-based decoupled impedance modeling method for DFIG system

As aforementioned, due to the couplings between the RSC and the GSC, it is difficult to build the full-order impedance model of the DFIG system. In this section, a two-port-network-based decoupled impedance modeling method will be introduced to overcome this difficulty.

At first, a conventional impedance modeling method by ignoring the dc-link coupling is discussed briefly. The structure of a real DFIG system is shown in Fig. 5(a), which can be treated as a two-port network. Due to the RSC and the GSC are coupled on both dc-side and ac-side, it is hard to build a full-order impedance model of the DFIG system. To address this difficulty, an approximate modeling method by ignoring the dc-link coupling is usually used, as shown in Fig. 5(b). Thus, the original two-port network can be simplified to be two one-port networks approximately. For the one-port network, it is easy to derive the output admittance according to the output voltages and currents. Thus, the output terminal admittance of the DFIG system can be derived by (8).

$$\mathbf{Y_{DFIG-SYS}}(s) \approx \mathbf{Y}'_{DFIG-SYS}(s) = \frac{-\Delta \mathbf{i_A}(s)}{\Delta \mathbf{v_A}(s)} + \frac{-\Delta \mathbf{i_B}(s)}{\Delta \mathbf{v_B}(s)} \tag{8}$$

However, the modeling method by ignoring the dc-link coupling is just an approximate method. To obtain an accurate full-order impedance/admittance model, the dc-link coupling should be considered. To describe the coupling between port A and port B, a 2×2 matrix is introduced in this paper. From the two-port network point of view, the relationship between voltages and currents at two ports can be described by a 2×2 admittance matrix, as expressed in (9). Thus, the admittance model of DFIG + RSC is represented by $\mathbf{Y_{AA}}$, and the admittance model of the GSC is represented by $\mathbf{Y_{BB}}$. Besides, the admittance model of the dc-link coupling between the GSC and RSC is represented by $\mathbf{Y_{AB}}$ and $\mathbf{Y_{BA}}$.

Fig. 2. Small-signal impedance model of DFIG in the d-q frame.
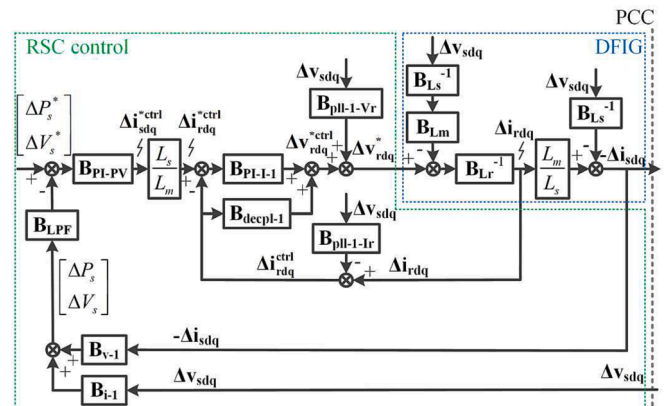

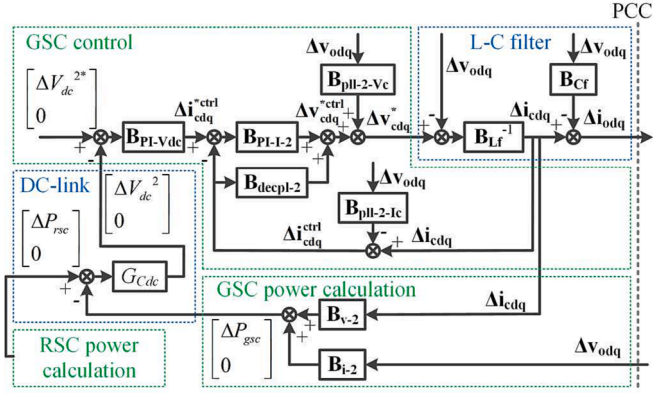**Fig. 3.** Small-signal impedance model of DFIG + RSC in the d-q frame.

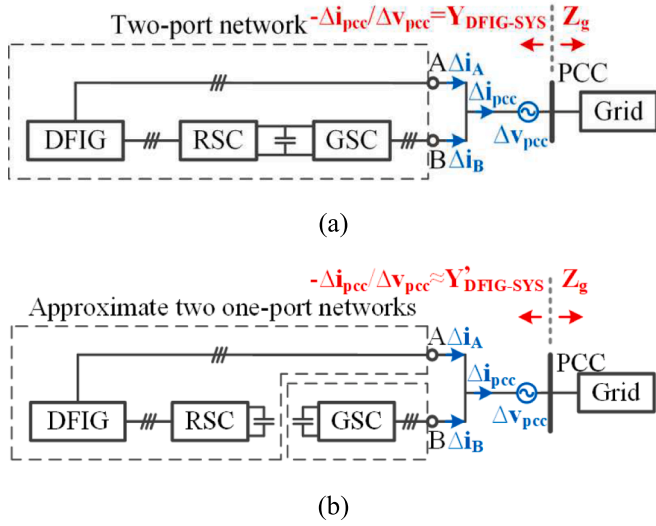Fig. 4. Small-signal impedance model of GSC in the d-q frame.

Fig. 5. Port network analysis of a normal DFIG system and an approximate DFIG system by ignoring the dc-link coupling. (a) A normal DFIG system; (b) An approximate DFIG system for modeling.

$$\begin{bmatrix} -\mathbf{\Delta i_A}(s) \\ -\mathbf{\Delta i_B}(s) \end{bmatrix} = \begin{bmatrix} \mathbf{Y_{AA}}(s) & \mathbf{Y_{AB}}(s) \\ \mathbf{Y_{BA}}(s) & \mathbf{Y_{BB}}(s) \end{bmatrix} \cdot \begin{bmatrix} \mathbf{\Delta v_A}(s) \\ \mathbf{\Delta v_B}(s) \end{bmatrix} \tag{9}$$

According to Fig. 5(a), it is known that "$\mathbf{\Delta i_{pcc}} = \mathbf{\Delta i_A} + \mathbf{\Delta i_B}$ and $\mathbf{\Delta v_{pcc}} = \mathbf{\Delta v_A} = \mathbf{\Delta v_B}$". Thus, the total output admittance of the DFIG system can be derived by (10), which is equal to the sum of four admittance components. Thus, as long as the four admittance components can be calculated, the total output admittance $\mathbf{Y_{DFIG\text{-}SYS}}$ can be obtained accordingly.

$$\begin{aligned} \mathbf{Y_{DFIG\text{-}SYS}}(s) &= \frac{-\mathbf{\Delta i_{pcc}}(s)}{\mathbf{\Delta v_{pcc}}(s)} = \frac{-[\mathbf{\Delta i_A}(s) + \mathbf{\Delta i_B}(s)]}{\mathbf{\Delta v_{pcc}}(s)} \\ &= \frac{[\mathbf{Y_{AA}\Delta v_A}(s) + \mathbf{Y_{AB}\Delta v_B}(s)] + [\mathbf{Y_{BA}\Delta v_A}(s) + \mathbf{Y_{BB}\Delta v_B}(s)]}{\mathbf{\Delta v_{pcc}}(s)} \\ &= \mathbf{Y_{AA}}(s) + \mathbf{Y_{AB}}(s) + \mathbf{Y_{BA}}(s) + \mathbf{Y_{BB}}(s) \end{aligned} \tag{10}$$

In order to calculate the four admittance components in (9), a two-port-network-based decoupled impedance modeling method is proposed in this paper, which is shown in Fig. 6. The main idea of the proposed method is to decouple the ac-side connection of port A and port B. Namely, port A and port B are connected to two grids ideally with the same parameters. Thus, each admittance component can be calculated or measured independently. It is worth mentioning that as long as the two grid voltages at the PCC and PCC' are the same, the modified DFIG system in Fig. 6 is equivalent to the original DFIG system in Fig. 5
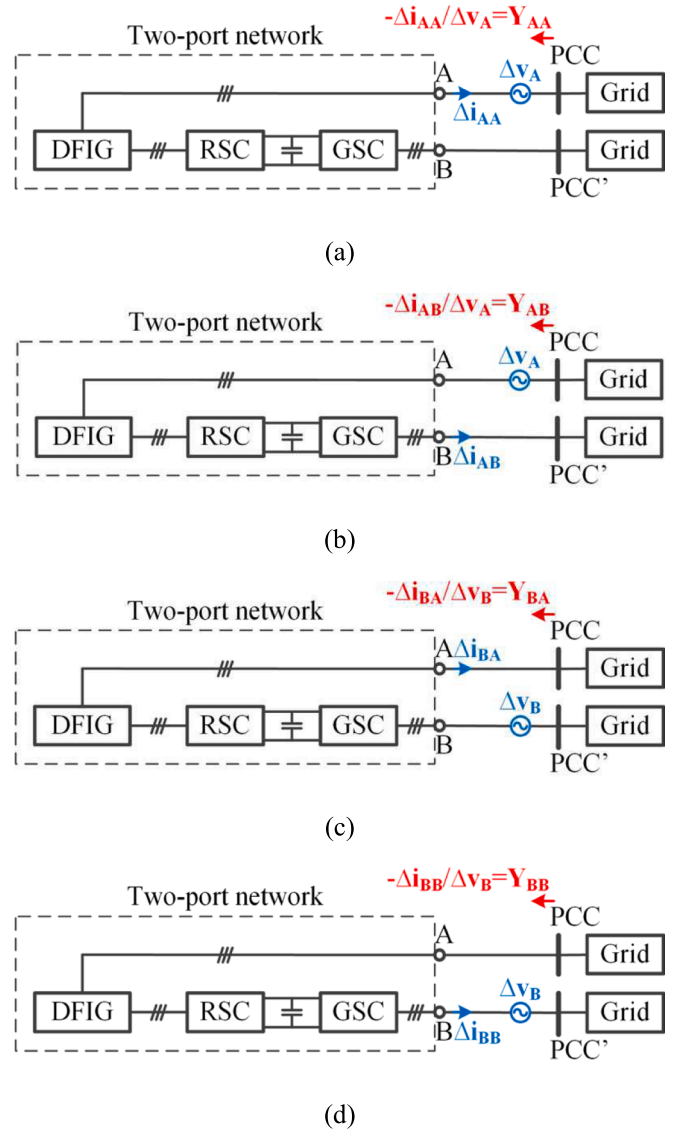
Fig. 6. Proposed two-port-network-based decoupled impedance modeling method for the DFIG system. (a) Modeling from port A to port A. (b) Modeling from port A to port B. (c) Modeling from port B to port A. (d) Modeling from port B to port B.

(a). The detailed admittance modeling process will be introduced in the following sections.

3.1. Admittance modeling from port A to port A

As shown in Fig. 6(a), when injecting a small-signal voltage perturbation $\mathbf{\Delta v_A}$ into the two-port network from port A, there is a current response $\mathbf{\Delta i_{AA}}$ at port A. So, the admittance $\mathbf{Y_{AA}}$ can be expressed as:

$$\mathbf{Y_{AA}^{dq}}(s) = \frac{-\mathbf{\Delta i_{AA}^{dq}}(s)}{\mathbf{\Delta v_A^{dq}}(s)} = \frac{\mathbf{\Delta i_{sdq}}(s)}{\mathbf{\Delta v_{sdq}}(s)} \tag{11}$$

where $\mathbf{\Delta i_{sdq}}$ and $\mathbf{\Delta v_{sdq}}$ are the stator current and voltage.

According to (11) and Fig. 3, the admittance $\mathbf{Y_{AA}}$ in Fig. 6(a) can be derived as:

$$\mathbf{Y_{AA}^{dq}}(s) = \left[\frac{L_s}{L_m}\left(\mathbf{B_{PI-I-1}} - \mathbf{B_{decpl-1}} + \mathbf{B_{Lr}} + \mathbf{B_{PI-I-1}}\mathbf{B_{PI-PV}}\mathbf{B_{LPF}}\mathbf{B_{v-1}}\right)\right]^{-1} \cdot \left[\mathbf{B_{Lm}}\mathbf{B_{Ls}^{-1}}\right.$$
$$- \left(\mathbf{B_{PI-I-1}} - \mathbf{B_{decpl-1}}\right)\mathbf{B_{pll-1-Ir}} - \mathbf{B_{pll-1-Vr}} + \frac{L_s}{L_m}\cdot\left(\mathbf{B_{PI-I-1}} - \mathbf{B_{decpl-1}} + \mathbf{B_{Lr}}\right)\mathbf{B_{Ls}^{-1}}$$
$$\left. + \frac{L_s}{L_m}\left(\mathbf{B_{PI-I-1}}\mathbf{B_{PI-PV}}\mathbf{B_{LPF}}\mathbf{B_{i-1}}\right)\right] \tag{12}$$

3.2. Admittance modeling from port A to port B

As shown in Fig. 6(b), when injecting a small-signal voltage perturbation $\mathbf{\Delta v_A}$ into the two-port network from port A, there is a current

$$\mathbf{Y_{AB}^{dq}}(s) = \frac{-3}{2}\cdot\left(\mathbf{B_{Lf}} + \mathbf{B_{PI-I-2}} - \mathbf{B_{decpl-2}} - \mathbf{B_{PI-I-2}}\mathbf{B_{PI-Vdc}}G_{Cdc}\mathbf{B_{v-2}}\right)^{-1}\cdot\left(\mathbf{B_{PI-I-2}}\mathbf{B_{PI-Vdc}}G_{Cdc}\right)\cdot\left\{\left[\frac{\left(L_m^2 - L_sL_r\right)s - 2R_rL_s}{L_m}\right.\right.$$

$$\left.\left.\cdot\begin{bmatrix} i_{rd0} & i_{rq0} \\ 0 & 0 \end{bmatrix} - \frac{\omega_{slip}}{\omega_1}\cdot\begin{bmatrix} v_{sd0} & v_{sq0} \\ 0 & 0 \end{bmatrix}\right]\cdot\mathbf{Y_{AA}^{dq}}(s) + \left[\frac{L_rs + 2R_r}{L_m}\cdot\begin{bmatrix} i_{rd0} & i_{rq0} \\ 0 & 0 \end{bmatrix} + \omega_{slip}\cdot\begin{bmatrix} -i_{sq0} & i_{sd0} \\ 0 & 0 \end{bmatrix}\right]\cdot\begin{bmatrix} s & -\omega_1 \\ \omega_1 & s \end{bmatrix}^{-1}\right\} \tag{18}$$

response $\mathbf{\Delta i_{AB}}$ at port B due to the dc-link coupling. So, the admittance $\mathbf{Y_{AB}}$ can be expressed as:

$$\mathbf{Y_{AB}^{dq}}(s) = \frac{-\mathbf{\Delta i_{AB}^{dq}}(s)}{\mathbf{\Delta v_A^{dq}}(s)} = \frac{-\mathbf{\Delta i_{odq}}(s)}{\mathbf{\Delta v_{sdq}}(s)} \tag{13}$$

where $\mathbf{\Delta i_{odq}}$ is the output current of the GSC and $\mathbf{\Delta v_{sdq}}$ is the stator voltage of the DFIG.

According to Fig. 4, assuming that the voltage $\mathbf{\Delta v_{odq}}$ is equal to zero, the transfer function from ΔP_{rsc} to $\mathbf{\Delta i_{odq}}$ can be derived as:

$$\mathbf{\Delta i_{odq}}(s) = -\left(\mathbf{B_{Lf}} + \mathbf{B_{PI-I-2}} - \mathbf{B_{decpl-2}} - \mathbf{B_{PI-I-2}}\mathbf{B_{PI-Vdc}}G_{Cdc}\mathbf{B_{v-2}}\right)^{-1}\cdot$$
$$\left(\mathbf{B_{PI-I-2}}\mathbf{B_{PI-Vdc}}G_{Cdc}\right)\cdot\begin{bmatrix} \Delta P_{rsc} \\ 0 \end{bmatrix} \tag{14}$$

If the switching losses on the RSC are ignored, the output power of the RSC is the same as the output power of the DFIG on the rotor side. Thus, the small-signal expression of the power ΔP_{rsc} is given by (15).

$$\begin{bmatrix} \Delta P_{rsc} \\ 0 \end{bmatrix} = -\frac{3}{2}\cdot\left\{\begin{bmatrix} i_{rd0} & i_{rq0} \\ 0 & 0 \end{bmatrix}\cdot\begin{bmatrix} \Delta v_{rd} \\ \Delta v_{rq} \end{bmatrix} + \begin{bmatrix} v_{rd0} & v_{rq0} \\ 0 & 0 \end{bmatrix}\cdot\begin{bmatrix} \Delta i_{rd} \\ \Delta i_{rq} \end{bmatrix}\right\} \tag{15}$$

where the subscript '$_0$' denotes the steady-state operating points of variables.

Substituting the small-signal expressions and the steady-state expressions of (1), (3) and (5) into (15), the power ΔP_{rsc} can be deduced as:

$$\begin{bmatrix} \Delta P_{rsc} \\ 0 \end{bmatrix} = -\frac{3}{2}\cdot\left\{\left[\frac{\left(L_m^2 - L_sL_r\right)s - 2R_rL_s}{L_m}\cdot\begin{bmatrix} i_{rd0} & i_{rq0} \\ 0 & 0 \end{bmatrix} - \frac{\omega_{slip}}{\omega_1}\cdot\begin{bmatrix} v_{sd0} & v_{sq0} \\ 0 & 0 \end{bmatrix}\right]\cdot\begin{bmatrix} \Delta i_{sd} \\ \Delta i_{sq} \end{bmatrix}\right.$$
$$\left. + \left[\frac{L_rs + 2R_r}{L_m}\cdot\begin{bmatrix} i_{rd0} & i_{rq0} \\ 0 & 0 \end{bmatrix} + \omega_{slip}\cdot\begin{bmatrix} -i_{sq0} & i_{sd0} \\ 0 & 0 \end{bmatrix}\right]\cdot\begin{bmatrix} s & -\omega_1 \\ \omega_1 & s \end{bmatrix}^{-1}\cdot\begin{bmatrix} \Delta v_{sd} \\ \Delta v_{sq} \end{bmatrix}\right\} \tag{16}$$

According to (11), $\mathbf{\Delta i_{sdq}}$ can be expressed by "$\mathbf{Y_{AA}}\bullet\mathbf{\Delta v_{sdq}}$". Thus, (16) can be deduced as (17).

$$\begin{bmatrix} \Delta P_{rsc} \\ 0 \end{bmatrix} = -\frac{3}{2}\cdot\left\{\left[\frac{\left(L_m^2 - L_sL_r\right)s - 2R_rL_s}{L_m}\cdot\begin{bmatrix} i_{rd0} & i_{rq0} \\ 0 & 0 \end{bmatrix} - \frac{\omega_{slip}}{\omega_1}\cdot\begin{bmatrix} v_{sd0} & v_{sq0} \\ 0 & 0 \end{bmatrix}\right]\cdot\mathbf{Y_{AA}^{dq}}(s)\right.$$
$$\left. + \left[\frac{L_rs + 2R_r}{L_m}\cdot\begin{bmatrix} i_{rd0} & i_{rq0} \\ 0 & 0 \end{bmatrix} + \omega_{slip}\cdot\begin{bmatrix} -i_{sq0} & i_{sd0} \\ 0 & 0 \end{bmatrix}\right]\cdot\begin{bmatrix} s & -\omega_1 \\ \omega_1 & s \end{bmatrix}^{-1}\right\}\cdot\mathbf{\Delta v_{sdq}}(s) \tag{17}$$

Substituting (14) and (17) into (13), the admittance $\mathbf{Y_{AB}}$ can be derived as:

3.3. Admittance modeling from port B to port A

As shown in Fig. 6(c), when injecting a small-signal voltage perturbation $\mathbf{\Delta v_B}$ into the two-port network from port B, there is a current response $\mathbf{\Delta i_{BA}}$ at port A. So, the admittance $\mathbf{Y_{BA}}$ can be expressed as:

$$\mathbf{Y_{BA}^{dq}}(s) = \frac{-\mathbf{\Delta i_{BA}^{dq}}(s)}{\mathbf{\Delta v_B^{dq}}(s)} = \frac{-\mathbf{\Delta i_{sdq}}(s)}{\mathbf{\Delta v_{odq}}(s)} \tag{19}$$

where $\mathbf{\Delta i_{sdq}}$ is the stator current of the DFIG and $\mathbf{\Delta v_{odq}}$ is the output voltage of the GSC.

Notably, the dc-link voltage is controlled by the GSC and the measured value of dc-link voltage is used for the voltage modulation on the RSC, so the output voltage of the RSC is independent from the dc-link voltage [29]. Thus, the injected small-signal perturbation at port B is only able to be transferred to the dc-link, while it cannot be further transferred to port A. So, $\mathbf{\Delta i_{BA}}$ is equal to zero theoretically. Thus, the admittance $\mathbf{Y_{BA}}$ in (19) can be derived as:

$$\mathbf{Y_{BA}^{dq}}(s) = \frac{\mathbf{0}}{\mathbf{\Delta v_B^{dq}}(s)} = \mathbf{0} \tag{20}$$

3.4. Admittance modeling from port B to port B

As shown in Fig. 6(d), when injecting a small-signal voltage perturbation $\mathbf{\Delta v_B}$ into the two-port network from port B, there is a current response $\mathbf{\Delta i_{BB}}$ at port B. So, the admittance $\mathbf{Y_{BB}}$ can be expressed as:

$$\mathbf{Y_{BB}^{dq}}(s) = \frac{-\mathbf{\Delta i_{BB}^{dq}}(s)}{\mathbf{\Delta v_B^{dq}}(s)} = \frac{-\mathbf{\Delta i_{odq}}(s)}{\mathbf{\Delta v_{odq}}(s)} \tag{21}$$

where $\mathbf{\Delta i_{odq}}$ and $\mathbf{\Delta v_{odq}}$ are the current and voltage of the GSC.

According to the small-signal model in Fig. 4, when the power ΔP_{rsc} is equal to zero, the expression of the current $\mathbf{\Delta i_{odq}}$ can be derived as:
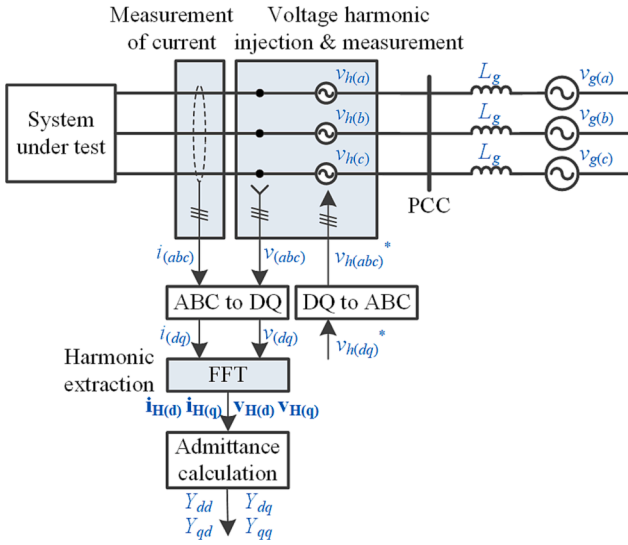
Fig. 7. A typical d-q impedance/admittance modeling system.

Table 1
Parameters of DFIG and RSC.

Parameters		Values
P_{N1}	Rated active power (3 phase)	2 MW (1 p.u.)
V_{N1}	Rated phase voltage, peak value	563 V (1 p.u.)
I_{N1}	Rated phase current, peak value	2368 A (1 p.u.)
f_1	Fundamental frequency	50 Hz (1 p.u.)
ω_1	Fundamental angular frequency	2π•50 rad/s (1p.u.)
ω_r	Rotor speed	40–60 Hz
n_p	Pole pairs	2
$L_{\sigma s}$	Stator leakage inductance	0.038 mH (0.05 p.u.)
$L_{\sigma r}$	Rotor leakage inductance	0.064 mH (0.08 p.u.)
L_m	Mutual inductance	2.9 mH (3.83 p.u.)
R_s	Stator resistance	1.7 mΩ (0.007 p.u.)
R_r	Rotor resistance	1.5 mΩ (0.006 p.u.)
K_e	Turns ratio	1/3
ω_{i1}	Designed current-loop bandwidth	2000 rad/s
ω_p	Designed power-loop bandwidth	10 rad/s
ω_v	Designed ac voltage-loop bandwidth	50 rad/s
ω_{LPF}	Cut-off angular frequency of LPFs	300 rad/s
ζ_1	Damping ratio of PLL-1	1
ω_{n1}	Natural frequency of PLL-1	100 rad/s

$$\mathbf{\Delta i_{odq}}(s) = -\left(\mathbf{B_{Lf}} + \mathbf{B_{PI-I-2}} - \mathbf{B_{decpl-2}} - \mathbf{B_{PI-I-2}B_{PI-Vdc}}G_{Cdc}\mathbf{B_{v-2}}\right)^{-1} \cdot [\mathbf{I}$$
$$- \left(\mathbf{B_{PI-I-2}} - \mathbf{B_{decpl-2}}\right)\mathbf{B_{pll-1-Ic}} - \mathbf{B_{pll-1-Vc}}$$
$$- \mathbf{B_{PI-I-2}B_{PI-Vdc}}G_{Cdc}\mathbf{B_{i-2}}] \cdot \mathbf{\Delta v_{odq}}(s) - \mathbf{B_{Cf}} \cdot \mathbf{\Delta v_{odq}}(s)$$
$$(22)$$

Substituting (22) into (21), the admittance $\mathbf{Y_{BB}}$ can be deduced as:

$$\mathbf{Y_{BB}^{dq}}(s) = \left(\mathbf{B_{Lf}} + \mathbf{B_{PI-I-2}} - \mathbf{B_{decpl-2}} - \mathbf{B_{PI-I-2}B_{PI-Vdc}}G_{Cdc}\mathbf{B_{v-2}}\right)^{-1} \cdot [\mathbf{I}$$
$$- \left(\mathbf{B_{PI-I-2}} - \mathbf{B_{decpl-2}}\right)\mathbf{B_{pll-1-Ic}} - \mathbf{B_{pll-1-Vc}} - \mathbf{B_{PI-I-2}B_{PI-Vdc}}G_{Cdc}\mathbf{B_{i-2}}] + \mathbf{B_{Cf}}$$
$$(23)$$

Based on the above analysis, the four admittance components $\mathbf{Y_{AA}}$, $\mathbf{Y_{AB}}$, $\mathbf{Y_{BA}}$, and $\mathbf{Y_{BB}}$ are obtained in (12), (18), (20), and (23). According to (10), the total admittance can also be obtained as "$\mathbf{Y_{DFIG-SYS}} = \mathbf{Y_{AA}} + \mathbf{Y_{AB}} + \mathbf{Y_{BA}} + \mathbf{Y_{BB}}$".

3.5. Validation by admittance measurement in the d-q frame

To verify the correctness of the proposed impedance modeling

Table 2
Parameters of GSC and Grid.

Parameters		Values
P_{N2}	Rated active power (3 phase)	667 kW (1/3 p.u.)
V_{N2}	Rated phase voltage, peak value	563 V (1 p.u.)
I_{N2}	Rated phase current, peak value	789 A (1/3 p.u.)
V_{dc}	Rated dc-link voltage	1.1 kV (1.95 p.u.)
C_{dc}	Dc-link capacitance	10 mF (2.25/3 p.u.)
L_f	Filter inductance	0.34 mH (0.15 × 3 p.u.)
R_f	Filter resistance	3.6 mΩ (0.005 × 3 p.u.)
C_f	Filter capacitance	75 μF (0.017/3 p.u.)
ω_{i2}	Designed current-loop bandwidth	2000 rad/s
ζ_{vdc}	Damping ratio of dc voltage loop	1
ω_{nvdc}	Natural frequency of dc voltage loop	40 rad/s
ζ_2	Damping ratio of PLL-2	1
ω_{n2}	Natural frequency of PLL-2	200 rad/s
SCR	Short-circuit ratio	1.5–15
L_g	Grid inductance	0.5–0.05 mH

method, a 2 MW grid-connected DFIG simulation model is built in Matlab/Simulink. Besides, a typical impedance/admittance measurement method introduced in [30] is used in this paper, which is shown in Fig. 7. It can be seen from Fig. 7 that small-signal harmonic perturbations $v_{h(abc)}$ are injected into the study system at the PCC. Meanwhile, the terminal voltage $v_{(abc)}$ and current $i_{(abc)}$ are measured by the voltage and current sensors. According to the measured voltage and current, the harmonic current and voltage components $\mathbf{i_{H(d)}}$, $\mathbf{i_{H(q)}}$, $\mathbf{v_{H(d)}}$ and $\mathbf{v_{H(q)}}$ can be extracted by using the fast Fourier transform (FFT) algorithm. Then, a 2 × 2 admittance matrix $[Y_{dd}, Y_{dq}; Y_{qd}, Y_{qq}]$ can be calculated accordingly. Moreover, this admittance modeling system can be simply extended to be used for the proposed two-port network-based decoupled DFIG system by placing the "Voltage harmonic injection" block and the "Measurement of current" block at different positions (i.e., four cases shown in Fig. 6).

The system and control parameters of the DFIG, RSC, and GSC are listed in Tables 1 and 2. The d-q admittance measurement results of the DFIG system under super-synchronous and sub-synchronous speed conditions are shown in Fig. 8, where the subscripts 'calc' and 'meas' of variables denote calculation and measurement respectively.

In Fig. 8, the red, green, and blue curves show the d-q admittance characteristics of $\mathbf{Y_{AA}}$, $\mathbf{Y_{AB}}$, and $\mathbf{Y_{BB}}$, which are calculated by (12), (18), and (23). Since $\mathbf{Y_{BA}}$ is equal to zero according to (20), it is omitted. Besides, the black curves show the admittance characteristics of $\mathbf{Y_{DFIG-SYS}}$, which is equal to the sum of $\mathbf{Y_{AA}}$, $\mathbf{Y_{AB}}$, $\mathbf{Y_{BA}}$, and $\mathbf{Y_{BB}}$. It can be seen from Fig. 8 that the calculated d-q admittance curves of $\mathbf{Y_{AA}}$, $\mathbf{Y_{AB}}$, $\mathbf{Y_{BB}}$ and $\mathbf{Y_{DFIG-SYS}}$ agree well with the measurement results, which proves the proposed two-port-network-based decoupled modeling method is correct.

As shown in Fig. 8, the impact of the dc-link coupling is more critical in the low-frequency range (e.g., lower than 100 Hz), because the magnitude of $\mathbf{Y_{AB}}$ relatively higher (closer to the magnitude of $\mathbf{Y_{DFIG-SYS}}$). Besides, by comparing Fig. 8(a) and (b), it can be seen that the impact of the dc-link coupling under the super-synchronous speed condition is stronger than that under sub-synchronous speed condition due to a higher magnitude of $\mathbf{Y_{AB}}$.

4. Dc-link coupling analysis

According to the admittance model of the DFIG system introduced in the previous section, it is known that the dc-link coupling can be reflected by the non-diagonal elements $\mathbf{Y_{AB}}$ and $\mathbf{Y_{BA}}$. Moreover, since the admittance $\mathbf{Y_{BA}}$ is equal to zero, the dc-link coupling is only reflected by the admittance $\mathbf{Y_{AB}}$. Hence, the impact of $\mathbf{Y_{AB}}$ will be mainly discussed in this section.
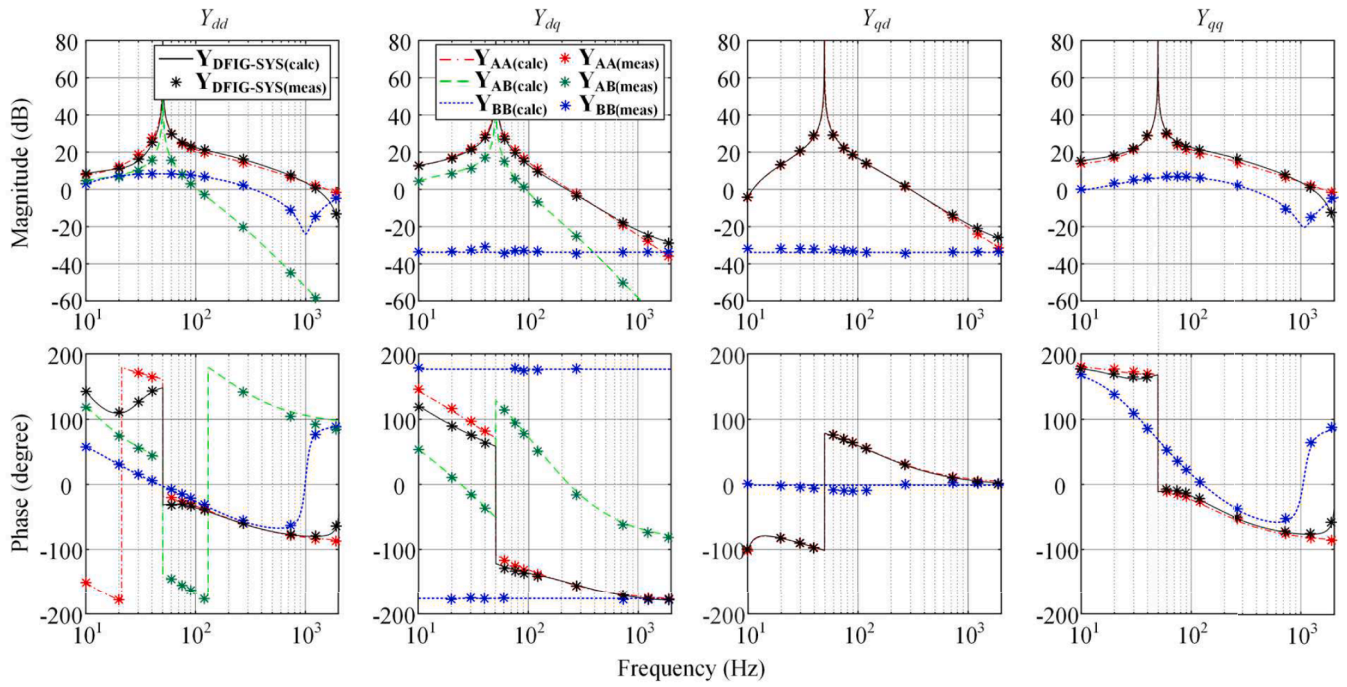
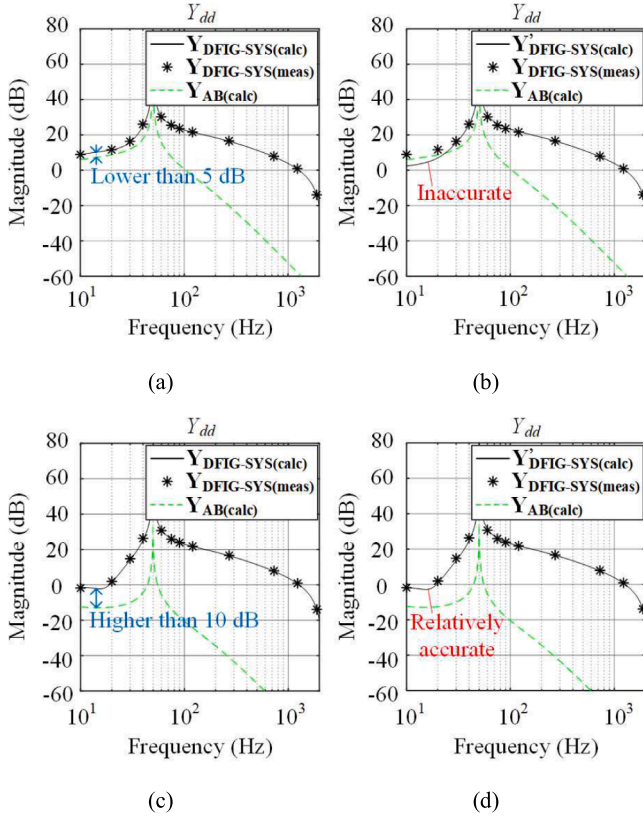(a)
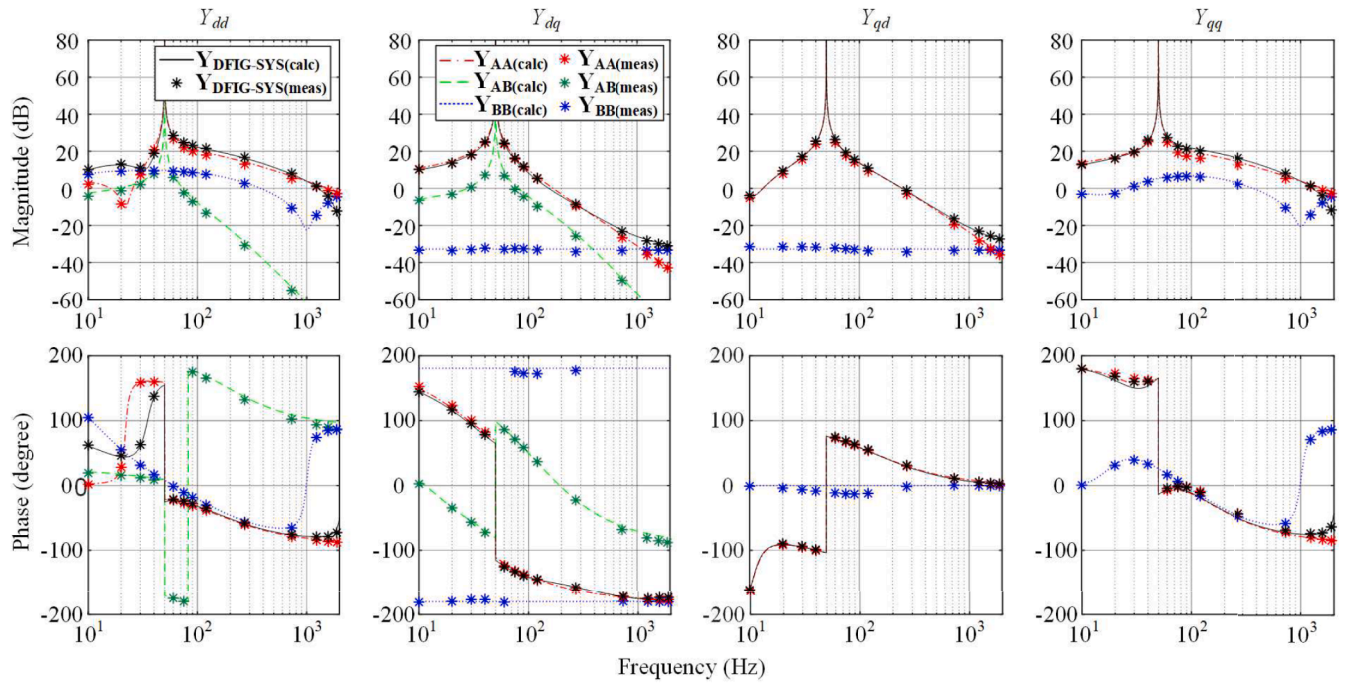
(b)

Fig. 8. Model validation by admittance measurement in the d-q frame. (a) Under super-synchronous speed condition with $\omega_r = 60$ Hz. (b) Under sub-synchronous speed condition with $\omega_r = 40$ Hz.
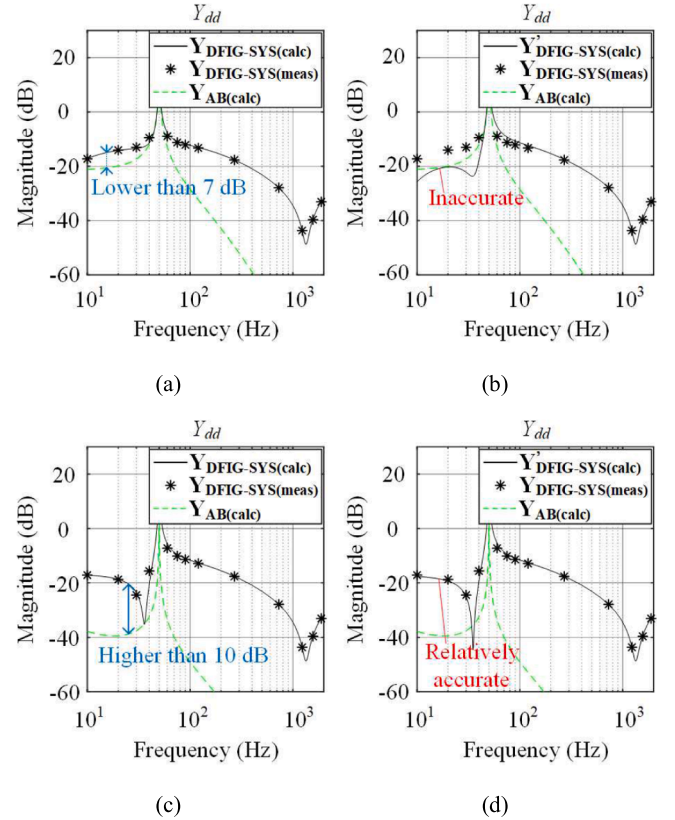
Fig. 9. Evaluation of the accuracy of the approximate model in case of 2 MW DFIG system. (a) Full-order model with $\mathbf{Y_{DFIG\text{-}SYS}} = \mathbf{Y_{AA}} + \mathbf{Y_{AB}} + \mathbf{Y_{BA}} + \mathbf{Y_{BB}}$. (b) Reduced-order model with $\mathbf{Y'_{DFIG\text{-}SYS}} = \mathbf{Y_{AA}} + \mathbf{Y_{BB}}$ (dc voltage loop bandwidth is 100 rad/s). (c) Full-order model with $\mathbf{Y_{DFIG\text{-}SYS}} = \mathbf{Y_{AA}} + \mathbf{Y_{AB}} + \mathbf{Y_{BA}} + \mathbf{Y_{BB}}$. (d) Reduced-order model with $\mathbf{Y'_{DFIG\text{-}SYS}} = \mathbf{Y_{AA}} + \mathbf{Y_{BB}}$ (dc voltage loop bandwidth is 10 rad/s).

Fig. 10. Evaluation of the accuracy of the approximate model in case of 30 kW DFIG system. (a) Full-order model with $\mathbf{Y_{DFIG\text{-}SYS}} = \mathbf{Y_{AA}} + \mathbf{Y_{AB}} + \mathbf{Y_{BA}} + \mathbf{Y_{BB}}$. (b) Reduced-order model with $\mathbf{Y'_{DFIG\text{-}SYS}} = \mathbf{Y_{AA}} + \mathbf{Y_{BB}}$ (dc voltage loop bandwidth is 100 rad/s). (c) Full-order model with $\mathbf{Y_{DFIG\text{-}SYS}} = \mathbf{Y_{AA}} + \mathbf{Y_{AB}} + \mathbf{Y_{BA}} + \mathbf{Y_{BB}}$. (d) Reduced-order model with $\mathbf{Y'_{DFIG\text{-}SYS}} = \mathbf{Y_{AA}} + \mathbf{Y_{BB}}$ (dc voltage loop bandwidth is 10 rad/s).

By substituting (A10)-(A15) into (18), the expression of $\mathbf{Y_{AB}}$ is able to be rewritten as (24).

calculated results in Fig. 9(b) are not overlapped. Differently, it can be seen from Fig. 9(c) and (d) that when the magnitude difference between $\mathbf{Y_{DFIG\text{-}SYS}}$ and $\mathbf{Y_{AB}}$ is higher than 10 dB, the approximate model $\mathbf{Y'_{DFIG\text{-}}}$

$$\mathbf{Y^{dq}_{AB}}(s) = \frac{\frac{\omega_{i2}}{\omega_{i2}+s}\cdot\left(2\zeta_{vdc}\omega_{nvdc}s+\omega^2_{nvdc}\right)}{s^2+\frac{\omega_{i2}}{\omega_{i2}+s}\cdot\left(2\zeta_{vdc}\omega_{nvdc}s+\omega^2_{nvdc}\right)}\cdot\frac{1}{V_o}\cdot\begin{bmatrix}1 & 0\\0 & 0\end{bmatrix}\cdot\left\{\left[\frac{\left(L^2_m-L_sL_r\right)s-2R_rL_s}{-L_m}\cdot\begin{bmatrix}i_{rd0} & i_{rq0}\\0 & 0\end{bmatrix}\right.\right.$$

$$+\frac{\omega_{slip}}{\omega_1}\cdot\begin{bmatrix}v_{sd0} & v_{sq0}\\0 & 0\end{bmatrix}\right]\cdot\mathbf{Y^{dq}_{AA}}(s)+\left[\frac{L_rs+2R_r}{L_m}\cdot\begin{bmatrix}i_{rd0} & i_{rq0}\\0 & 0\end{bmatrix}+\omega_{slip}\cdot\begin{bmatrix}-i_{sq0} & i_{sd0}\\0 & 0\end{bmatrix}\right]\cdot\begin{bmatrix}s & -\omega_1\\\omega_1 & s\end{bmatrix}^{-1}\right\}$$

(24)

It can be seen from (24) that the magnitude of $\mathbf{Y_{AB}}$ is proportional to ω_{nvdc}. Notably, since the dc voltage control loop is a second-order system, when the damping ratio ζ_{vdc} is constant, the natural angular frequency ω_{nvdc} is proportional to the bandwidth [28]. Thus, the magnitude of $\mathbf{Y_{AB}}$ is also proportional to the bandwidth of the dc voltage control loop. Therefore, a higher bandwidth 100 rad/s and a lower bandwidth 10 rad/s of the dc voltage control loop are chosen as examples for analyzing the impact of $\mathbf{Y_{AB}}$, which are shown in Fig. 9(a), (b), and (c), (d) respectively.

It can be seen from Fig. 9(a) and (b) that when the magnitude difference between $\mathbf{Y_{DFIG\text{-}SYS}}$ and $\mathbf{Y_{AB}}$ is lower than 5 dB, the approximate model $\mathbf{Y'_{DFIG\text{-}SYS}}$ is inaccurate, because the measured results and the

$\mathbf{sys}$ is relatively accurate, because the measured results and the calculated results in Fig. 9(d) are almost overlapped.

Moreover, to see whether the above conclusion is suitable for a low-power DFIG system, the admittance characteristics of a 30 kW DFIG system is presented in Fig. 10.

It can be seen from Fig. 10(a) and (b) that when the magnitude difference between $\mathbf{Y_{DFIG\text{-}SYS}}$ and $\mathbf{Y_{AB}}$ is lower than 7 dB, the approximate model $\mathbf{Y'_{DFIG\text{-}SYS}}$ is inaccurate, because the measured results and the calculated results in Fig. 10(b) are not overlapped. Differently, it can be seen from Fig. 10(c) and (d) that when the magnitude difference between $\mathbf{Y_{DFIG\text{-}SYS}}$ and $\mathbf{Y_{AB}}$ is higher than 10 dB, the approximate model $\mathbf{Y'_{DFIG\text{-}SYS}}$ is relatively accurate, because the measured results and the calculated results in Fig. 10(d) are almost overlapped.
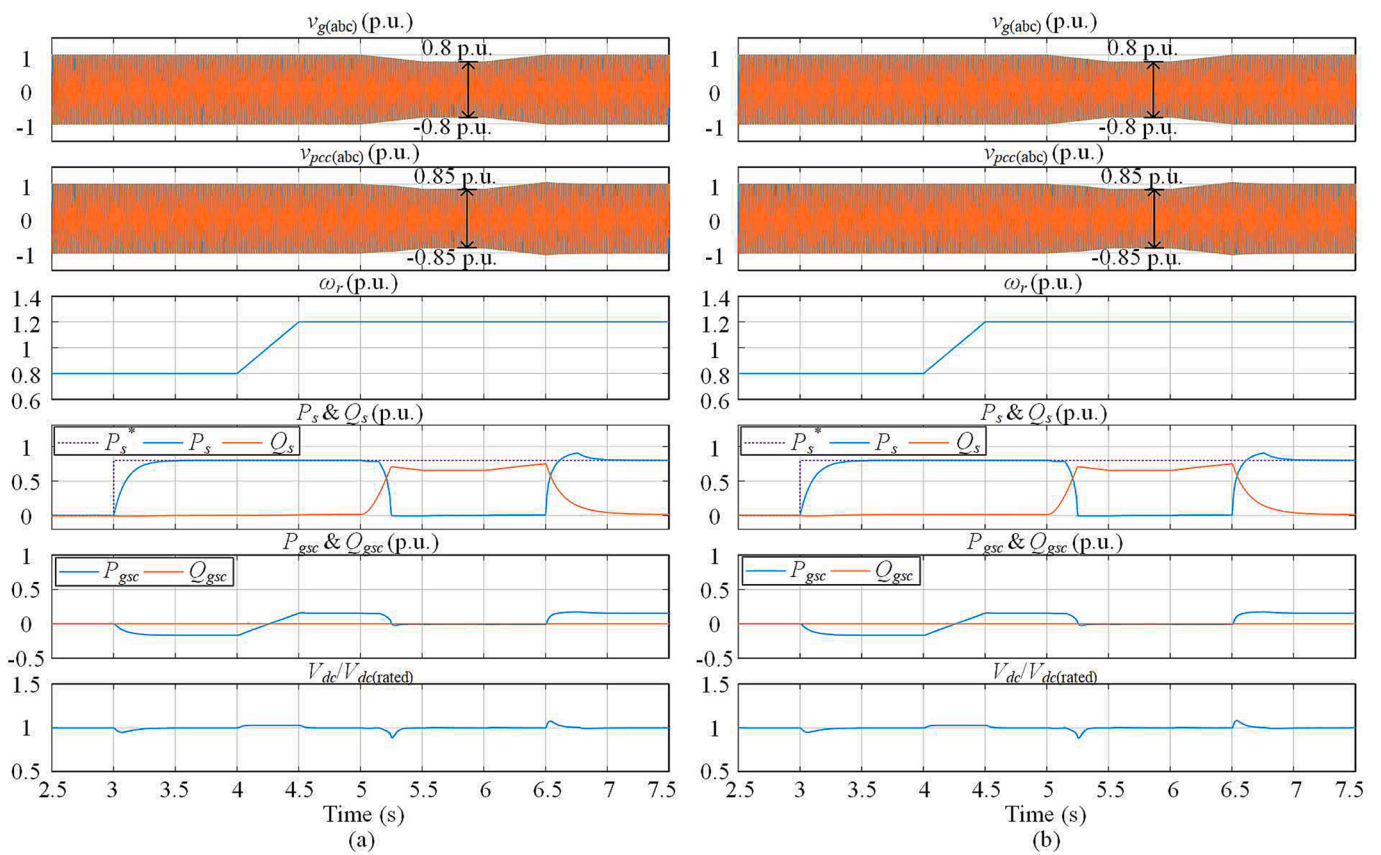
Fig. 11. Simulation results in a strong grid case (SCR = 15). (a) Normal DFIG system in Fig. 5. (b) Proposed decoupled DFIG system in Fig. 6.
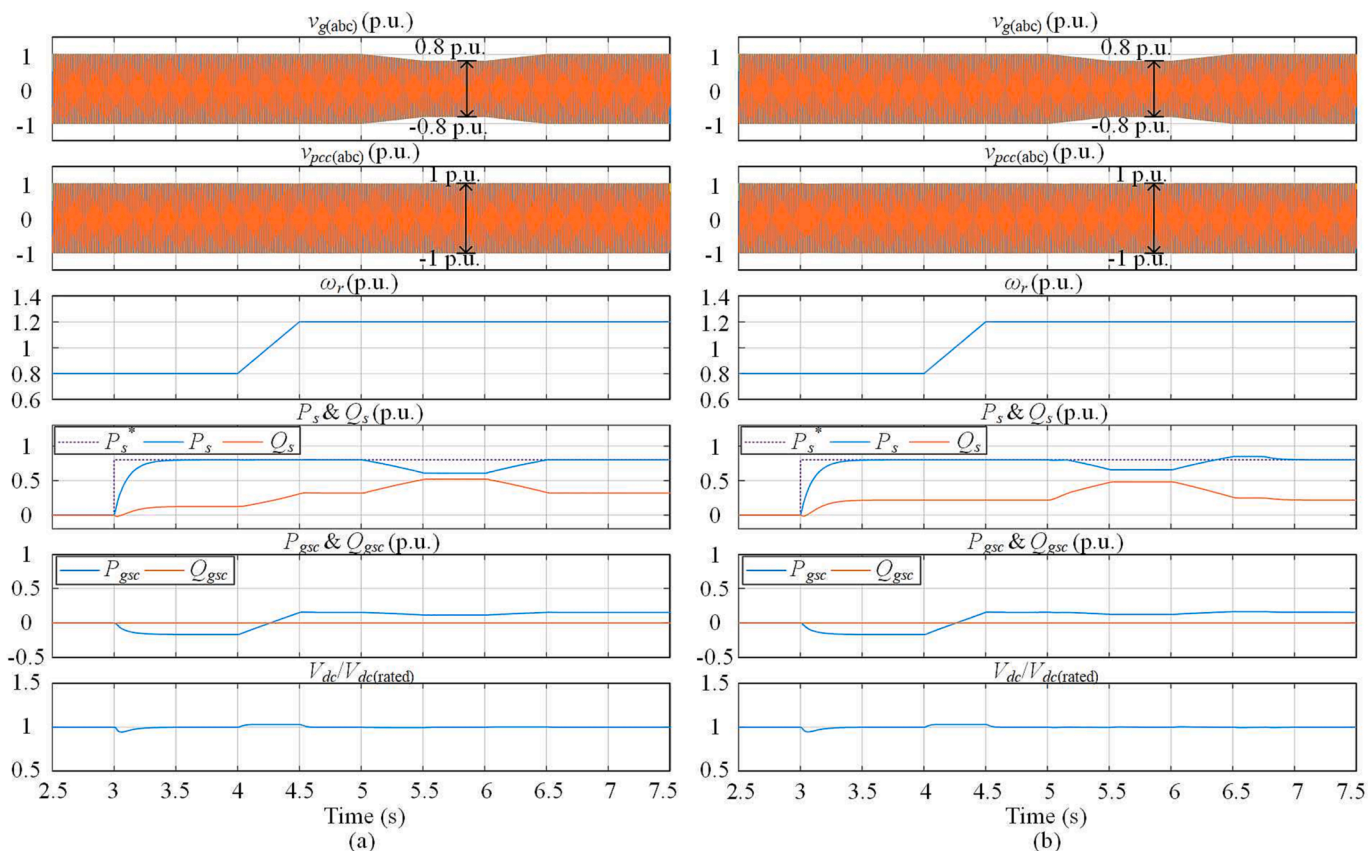
Fig. 12. Simulation results in a weak grid case (SCR = 1.5). (a) Normal DFIG system in Fig. 5. (b) Proposed decoupled DFIG system in Fig. 6.

Based on the above analysis, the critical condition for ignoring the dc-link voltage dynamics (i.e., the magnitude difference is at least 10 dB) revealed in this manuscript is suitable for both the high-power (e.g., 2 MW) DFIG system and the low-power (e.g., 30 kW) DFIG system.

5. Time-domain simulation comparison

In order to see the difference between the normal DFIG system and the proposed decoupled DFIG system, the time-domain simulation results will be compared in this section.

A strong grid case with SCR = 15 is provided in Fig. 11, where Fig. 11 (a) shows the simulation results of a normal DFIG system, while Fig. 11 (b) shows the simulation results of the proposed decoupled DFIG system. At the instant of 3 s, the stator active power reference is increased from 0 to 0.8 p.u. Then, the stator active power follows the reference to be increased to 0.8 p.u. During the time period 4 s–4.5 s, the rotor speed is increased from 0.8 p.u. to 1.2 p.u., and the active power of the GSC is changed from negative to positive. Afterward, during the time period 5 s–5.5 s, the grid voltage magnitude is reduced from 1p.u. to 0.8p.u. The stator reactive power is increased to support the PCC voltage, but the PCC voltage can only be supported to be 0.85 p.u. in the strong grid case. Then, when the grid voltage returns to its nominal value after 6.5 s, all the variables go back to the original steady-state values. It can be seen from Fig. 11 that the simulation results of a normal DFIG system and the proposed decoupled DFIG system are highly identical.

In addition, a weak grid case with SCR = 1.5 is provided in Fig. 12, where Fig. 12(a) presents the simulation results of a normal DFIG system, while Fig. 12(b) presents the simulation results of the proposed decoupled DFIG system. At the moment of 3 s, the stator active power reference is rised from 0 to 0.8 p.u. Then, the stator active power follows the reference. During the time period 4 s–4.5 s, the rotor speed is changed from 0.8 p.u. to 1.2 p.u., and the active power of the GSC is

changed from negative to positive. Afterward, during the time period 5 s–5.5 s, the grid voltage magnitude is decreased from 1 p.u. to 0.8 p.u. The stator reactive power is increased to support the PCC voltage and the magnitude of the PCC voltage is supported to be 1 p.u. in the weak grid case. Then, when the grid voltage returns to its nominal value after 6.5 s, all the variables go back to the original steady-state values. Overall, during the whole process, only the stator reactive powers in Fig. 12(a) and (b) are slightly different. Aside from that, other variables in Fig. 12(a) and (b) are basically identical.

Based on the above analysis, the proposed decoupled DFIG system shown in Fig. 6 can be considered to be equivalent to the normal DFIG system shown in Fig. 5.

Notably, since the research focus of this paper is the small-signal modeling, the transient performance under grid fault conditions is not considered in this paper, which will be studied further in our future work.

6. Conclusion

This paper introduces a two-port-network-based decoupled impedance modeling method for the DFIG system. By using this method, the total admittance of the DFIG system is decomposed into four admittance components. Each of them can be modeled separately, so that the complexity of the modeling process is degraded. Besides, since the dc-link coupling can be modeled separately, its impact on the whole DFIG system is able to be analyzed quantitatively and intuitively. Through the quantitative analysis, it is found that when the bandwidth of the dc voltage control loop is low enough to make the magnitudes of the coupling admittance at least 10 dB lower than that of the total admittance, the coupling effect caused by the dc-link voltage dynamics can be ignored. Otherwise, the dc-link voltage dynamics should be considered. Thus, the precondition of ignoring the dc-link voltage

dynamics is found in this paper. All the theoretical analyses are verified by admittance measurements in simulations.

CRediT authorship contribution statement

Liang Huang: Conceptualization, Methodology, Validation, Visualization, Writing – original draft. **Chao Wu:** Supervision, Writing – review & editing. **Dao Zhou:** Supervision, Writing – review & editing. **Frede Blaabjerg:** Funding acquisition, Supervision, Writing – review & editing.

Declaration of competing interest

The authors declare that they have no known competing financial interests or personal relationships that could have appeared to influence the work reported in this paper.

Data availability

No data was used for the research described in the article.

Appendix A

The 2 × 2 matrixes in the RSC impedance model shown in Fig. 3 are given by (A1)-(A8).

$$\mathbf{B_{PI-I-1}} = \begin{bmatrix} K_{p\_I\_rsc} + \dfrac{K_{i\_I\_rsc}}{s} & 0 \\ 0 & K_{p\_I\_rsc} + \dfrac{K_{i\_I\_rsc}}{s} \end{bmatrix} \tag{A1}$$

where $K_{p\_I\_rsc} + K_{i\_I\_rsc}/s = \omega_{i1}\sigma L_r + \omega_{i1}R_r/s$.

$$\mathbf{B_{decpl-1}} = \begin{bmatrix} 0 & -\omega_{slip}\sigma L_r \\ \omega_{slip}\sigma L_r & 0 \end{bmatrix} \tag{A2}$$

$$\mathbf{B_{PI-PV}} = \begin{bmatrix} K_{p\_P\_rsc} + \dfrac{K_{i\_P\_rsc}}{s} & 0 \\ 0 & -K_{p\_V\_rsc} - \dfrac{K_{i\_V\_rsc}}{s} \end{bmatrix} \tag{A3}$$

where $K_{p\_P\_rsc} + K_{i\_P\_rsc}/s = \omega_p/1.5/V_{N1}\bullet(1/\omega_{LPF} + 1/s)$.

$$\mathbf{B_{LPF}} = \begin{bmatrix} \dfrac{\omega_{LPF}}{s + \omega_{LPF}} & 0 \\ 0 & \dfrac{\omega_{LPF}}{s + \omega_{LPF}} \end{bmatrix} \tag{A4}$$

$$\mathbf{B_{v-1}} = \begin{bmatrix} 1.5v_{sd0} & 1.5v_{sq0} \\ 0 & 0 \end{bmatrix} \tag{A5}$$

$$\mathbf{B_{i-1}} = \begin{bmatrix} -1.5i_{sd0} & -1.5i_{sq0} \\ 1 & 0 \end{bmatrix} \tag{A6}$$

$$\mathbf{B_{pll-1-Vr}} = \begin{bmatrix} 0 & -v_{rq0}\cdot\dfrac{G_{pll-1}}{V_s} \\ 0 & v_{rd0}\cdot\dfrac{G_{pll-1}}{V_s} \end{bmatrix} \tag{A7}$$

where $G_{pll-1} = (2\zeta_1\omega_{n1}s + \omega_{n1}^2)/(s^2 + 2\zeta_1\omega_{n1}s + \omega_{n1}^2)$.

$$\mathbf{B_{pll-1-Ir}} = \begin{bmatrix} 0 & -i_{rq0}\cdot\dfrac{G_{pll-1}}{V_s} \\ 0 & i_{rd0}\cdot\dfrac{G_{pll-1}}{V_s} \end{bmatrix} \tag{A8}$$

The 2 × 2 matrixes in the GSC impedance model shown in Fig. 4 are given by (A9)-(A18).

$$\mathbf{B_{Cf}} = \begin{bmatrix} sC_f & -\omega_1 C_f \\ \omega_1 C_f & sC_f \end{bmatrix} \tag{A9}$$

$$\mathbf{B_{Lf}} = \begin{bmatrix} sL_f + R_f & -\omega_1 L_f \\ \omega_1 L_f & sL_f + R_f \end{bmatrix} \tag{A10}$$

$$\mathbf{B_{PI-I-2}} = \begin{bmatrix} K_{p\_I\_gsc} + \dfrac{K_{i\_I\_gsc}}{s} & 0 \\ 0 & K_{p\_I\_gsc} + \dfrac{K_{i\_I\_gsc}}{s} \end{bmatrix} \tag{A11}$$

where $K_{p\_I\_gsc} + K_{i\_I\_gsc}/s = \omega_{i2}L_f + \omega_{i2}R_f/s$.

$$\mathbf{B_{decpl-2}} = \begin{bmatrix} 0 & -\omega_1 L_f \\ \omega_1 L_f & 0 \end{bmatrix} \tag{A12}$$

$$\mathbf{B_{PI-Vdc}} = \begin{bmatrix} -K_{p\_Vdc\_gsc} - \dfrac{K_{i\_Vdc\_gsc}}{s} & 0 \\ 0 & 0 \end{bmatrix} \tag{A13}$$

where $K_{p\_Vdc\_gsc} + K_{i\_Vdc\_gsc}/s = C_{dc}/2/1.5/V_{N2}\bullet(2\zeta_{vdc}\omega_{nvdc} + \omega_{nvdc}^2/s)$.

$$G_{Cdc} = \frac{1}{(C_{dc}/2)s} \tag{A14}$$

$$\mathbf{B_{v-2}} = \begin{bmatrix} 1.5\cdot v_{od0} & 1.5\cdot v_{oq0} \\ 0 & 0 \end{bmatrix} \tag{A15}$$

$$\mathbf{B_{i-2}} = \begin{bmatrix} 1.5\cdot i_{cd0} & 1.5\cdot i_{cq0} \\ 0 & 0 \end{bmatrix} \tag{A16}$$

$$\mathbf{B_{pll-2-Vc}} = \begin{bmatrix} 0 & -v_{cq0}\cdot\dfrac{G_{pll-2}}{V_o} \\ 0 & v_{cd0}\cdot\dfrac{G_{pll-2}}{V_o} \end{bmatrix} \tag{A17}$$

where $G_{pll-2} = (2\zeta_2\omega_{n2}s + \omega_{n2}^2) / (s^2 + 2\zeta_2\omega_{n2}s + \omega_{n2}^2)$.

$$\mathbf{B_{pll-2-Ic}} = \begin{bmatrix} 0 & -i_{cq0}\cdot\dfrac{G_{pll-2}}{V_o} \\ 0 & i_{cd0}\cdot\dfrac{G_{pll-2}}{V_o} \end{bmatrix} \tag{A18}$$

References

[1] Blaabjerg F, Yang Y, Yang D, Wang X. Distributed power-generation systems and protection. Proc IEEE 2017;105:1311–31.

[2] Getting fit for 55 and set for 2050, European Technology & Innovation Platform on Wind Energy, Technical Report; 2021.

[3] Hvelplund F, Østergaard PA, Meyer NI. Incentives and barriers for wind power expansion and system integration in Denmark. Energy Policy 2017;107:573–84.

[4] Cheng Y, Fan L, Rose J, Huang F, Schmall J, Wang X, et al. Real-world subsynchronous oscillation events in power grids with high penetrations of inverter-based resources. IEEE Trans Power Syst (Early Access) 2022;38(1): 316–30.

[5] Fan L. Modeling type-4 wind in weak grids. IEEE Trans Sustain Energy 2019;10: 853–64.

[6] Suul JA, D'Arco S, Rodríguez P, Molinas M. Impedance-compensated grid synchronisation for extending the stability range of weak grids with voltage source converters. IET Gener Transm Distrib 2016;10:1315–26.

[7] Harnefors L. Modeling of three-phase dynamic systems using complex transfer functions and transfer matrices. IEEE Trans Ind Electron 2007;54:2239–48.

[8] Avazov A, Colas F, Beerten J, Guillaud X. Application of input shaping method to vibrations damping in a Type-IV wind turbine interfaced with a grid-forming converter. Electr Power Syst Res 2022;210:108083.

[9] Oraa I, Samanes J, Lopez J, Gubia E. Modeling of a droop-controlled grid-connected DFIG wind turbine. IEEE Access 2022;10:6966–77.

[10] Li Y, Fan L, Miao Z. Stability control for wind in weak grids. IEEE Trans Sustain Energy 2019;10:2094–103.

[11] Xu Y, Zhang M, Fan L, Miao Z. Small-signal stability analysis of type-4 wind in series-compensated networks. IEEE Trans Energy Convers 2020;35:529–38.

[12] Huang L, Wu C, Zhou D, Blaabjerg F. Comparison of DC-link voltage control schemes on grid-side and machine-side for type-4 wind generation system under weak grid. In: Toronto ON, editor. IECON 2021–47th annual conference of the IEEE industrial electronics society. Canada; 2021. p. 1–6.

[13] Pedra J, Sainz L, Monjo L. Comparison of small-signal admittance-based models of doubly-fed induction generators. Int J Electr Power Energy Syst 2023;145:108654.

[14] Zhang Y, Klabunde C, Wolter M. Frequency-coupled impedance modeling and resonance analysis of DFIG-based offshore wind farm with HVDC connection. IEEE Access 2020;8:147880–94.

[15] Qin S, Yang M, Zhang X, Ma Z, Zhao J, Xu D. Voltage disturbance compensation based on impedance modeling of DFIG under weak grid. Int J Electr Power Energy Syst 2021;131:107062.

[16] Hu J, Huang Y, Wang D, Yuan H, Yuan X. Modeling of grid-connected DFIG-based wind turbines for DC-link voltage stability analysis. IEEE Trans Sustain Energy 2015;6:1325–36.

[17] Xu Y, Nian H, Wang T, Chen L, Zheng T. Frequency coupling characteristic modeling and stability analysis of doubly fed induction generator. IEEE Trans Energy Convers 2018;33:1475–86.

[18] Hu B, Nian H, Li M, Liao Y, Yang J, Tong H. Impedance characteristic analysis and stability improvement method for DFIG system within PLL bandwidth based on different reference frames. IEEE Trans Ind Electron 2023;70:532–43.

[19] Vieto I, Sun J. Sequence impedance modeling and analysis of type-III wind turbines. IEEE Trans Energy Convers 2018;33:537–45.

[20] Jin W, Lu Y. Stability analysis and oscillation mechanism of the DFIG-based wind power system. IEEE Access 2019;7:88937–48.

[21] Sun K, Yao W, Fang J, Ai X, Wen J, Cheng S. Impedance modeling and stability analysis of grid-connected DFIG-based wind farm with a VSC-HVDC. IEEE J Emerg Sel Topics Power Electron 2020;8:1375–90.

[22] Zhang C, Cai X, Molinas M, Rygg A. Frequency-domain modelling and stability analysis of a DFIG-based wind energy conversion system under non-compensated AC grids: impedance modelling effects and consequences on stability. IET Power Electron 2019;12:907–14.

[23] Nian H, Xu Y, Chen L, Zhu M. Modeling and analysis of DC-link dynamics in DFIG system with an indicator function. IEEE Access 2019;7:125401–12.

[24] Sun J, Vieto I. Development and application of type-III turbine impedance models including DC bus dynamics. IEEE Open J Power Electron 2020;1:513–28.

[25] Mishra Y, Mishra S, Tripathy M, Senroy N, Dong ZY. Improving stability of a DFIG-based wind power system with tuned damping controller. IEEE Trans Energy Convers 2009;24(3):650–60.

[26] Prajapat GP, Senroy N, Kar IN. Small signal stability improvement of a grid connected DFIG through Quadratic Regulator. In: 2016 IEEE 6th International Conference on Power Systems (ICPS), New Delhi, India; 2016. p. 1–6.

[27] Boldea I. Induction machines handbook. CRC Press; 2020.

[28] Huang L, Wu C, Zhou D, Blaabjerg F. A double-PLLs-based impedance reshaping method for extending stability range of grid-following inverter under weak grid. IEEE Trans Power Electron 2022;37:4091–104.

[29] Xue T, Lyu J, Wang H, Cai X, Li J, Wang X. A complete impedance model of a PMSG-based wind turbine system considering machine-side dynamics. In: IECON 2020 The 46th Annual Conference of the IEEE Industrial Electronics Society, Singapore; 2020. p. 3111–7.

[30] Francis G, Burgos R, Boroyevich D, Wang F, Karimi K. An algorithm and implementation system for measuring impedance in the D-Q domain. In: IEEE energy conversion congress and exposition Phoenix, AZ, USA; 2011. p. 3221–8.